Rupture process during the 2007 Noto Hanto earthquake (M_{JMA} 6.9) and strong-motion simulation in the source region

Yoshiaki Shiba

Central Research Institute of Electric Power Industry, 1646 Abiko, Abiko-shi, Chiba 270-1194, Japan

(Received July 2, 2007; Revised May 8, 2008; Accepted July 1, 2008; Online published November 7, 2008)

The source rupture process during the 2007 Noto Hanto earthquake is inferred using a broadband waveform inversion technique based on the empirical Green's function and the simulated annealing. The spatio-temporal distributions of the moment density and rise time on the fault are estimated from displacement motions in the frequency range from 0.1 to 2 Hz, and effective stress distribution is derived from the velocity motions in the frequency range up to 5 Hz. Results from the displacement inversion indicate that the seismic moment is mainly released from a single asperity with an area of 10×10 km^2, and total moment release is estimated to be about 1.3×10^{19} N m. The velocity inversion shows that the high effective stress area distributes on and around the asperity, in particular at the deep periphery of it. The broadband strong motions determined using the conventional source model composed of only the moment distribution are compared with those calculated by considering both moment and effective stress separately. The fit between observed acceleration motions and synthetic ones from both source models are generally good in the frequency range up to 10 Hz, and no evident difference is recognized.
Key words: Rupture process, waveform inversion, strong ground motion, simulated annealing, empirical Green's function.

1. Introduction

The Noto-Hanto earthquake (M_{JMA} 6.9) occurred on 25 March 2007 on the Noto peninsula, Ishikawa prefecture on the Coast of the Japan Sea. Most of the main shock fault lies beneath the inland area, and some towns suffered severe damages. Since tens of strong-motion observation stations are distributed on and around the source area, installed by the National Research Institute for Earth Science and Disaster Prevention, called K-NET (Kinoshita, 1998) and KiK-net (Aoi *et al*., 2000), and by the Japan Meteorological Agency (JMA), this event is an appropriate case for investigating the detailed source rupture process generating strong motions, though the station coverage might not be satisfactory.

In this article I apply the source inversion scheme composed of the empirical Green's function method and simulated annealing (Shiba and Irikura, 2005) to broadband strong-motion data from the 2007 Noto Hanto earthquake and separately estimate the spatio-temporal distributions of the seismic moment and effective stress on the fault. Waveform fitting for the velocity motions in the frequency range up to 5 Hz is performed in order to directly infer the detailed source process radiating the high-frequency strong motions from the observed data. To represent the real rupture process, effective stress is added to the independent source parameters describing a variation of the slip velocity function on the fault, together with the seismic moment, rise time, and rupture time. I then compare the synthetic ground motions in the broadband frequency range (0.1 to 10 Hz) calculated from the source model estimated by proposed inversion method and those determined by the conventional method to reveal important parameters for predicting broadband strong ground motions.

2. Inversion Method

The inversion scheme used in this study is principally based on the method proposed by Shiba and Irikura (2005). This method is composed of the very fast simulated annealing (VFSA), which is one of the heuristic search algorithms used to statistically find the best global solution of a nonlinear nonconvex (multimodal) problem (Ingber, 1989; Kirkpatrick *et al*., 1983), and the empirical Green's function method (EGFM; Irikura, 1986) as a forward process to calculate synthetic ground motions. In order to examine the detailed source process radiating broadband, particularly high-frequency ground motions, I adopt two-step inversion scheme, in which displacement motions are first inverted to search the moment and rise time distributions with rupture times, and then velocity motions are compared with synthetic motions to find the effective stress distribution with fixed rise time and variable moment density. For the shape of the slip velocity function (exactly a filter function in the EGFM) on the fault, the displacement inversion employs a boxcar function with the height proportional to the seismic moment and the duration equivalent to the rise time. In contrast, the velocity inversion uses a combination of a delta function proportional to the effective stress and the boxcar function to satisfy the similarity law of source spectra, this is called the ω-square model (Aki, 1967) to the higher frequency range. The seismic moment and rise time

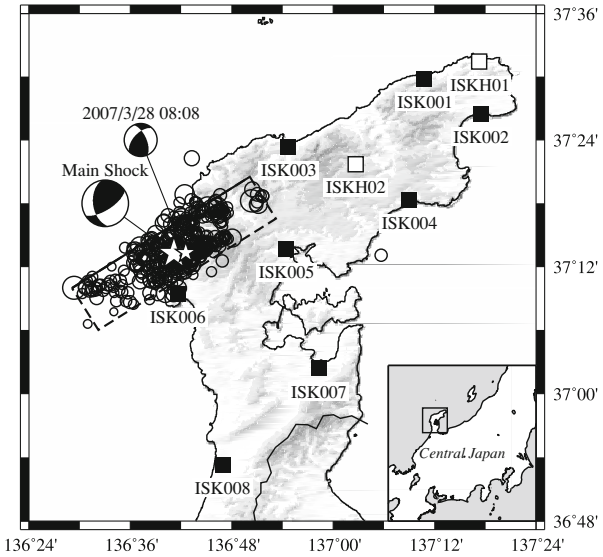

Fig. 1. Location map showing the strong-motion stations, initial fault model of the main shock, and epicenters of aftershocks. Solid and open squares show the K-NET and the KiK-net stations, respectively. Star symbols indicate epicenters of the main shock and the element event used as the empirical Green's function. Circles indicate the epicenters of aftershocks within 24 h after the main shock, and their sizes vary with the magnitude.

control low-frequency motions, while the effective stress and the variation of rupture times are strongly related to the high-frequency radiation. Therefore, the seismic moment and rise time distribution are estimated from the displacement motions before the search of effective stress variation by fitting the high-frequency velocity waveforms to ensure the stability of inversion results.

In this study I adopt some modifications or improvements to the proposed method of Shiba and Irikura (2005). A spatial smoothing constraint for all search parameters except rupture time is imposed to suppress the instability of solutions following Yoshida and Koketsu (1990) such as,

$$\nabla^2 X_{m,n} = X_{m+1,n} + X_{m,n+1} - 4X_{m,n} + X_{m-1,n} + X_{m,n-1} = 0 \quad (1)$$

where $X_{m,n}$ is a search parameter at the mn-th subfault, and ∇^2 is a discrete Laplacian operator. Suitable weights for the smoothing constraint are determined through Akaike's Bayesian Information Criterion (ABIC; Akaike, 1980). Rupture time variation obeys only the causality; that is, a subfault does not fail until its neighbor nearest to the rupture initiation point has failed (Ihmlé, 1996). Furthermore, in the velocity inversion, the rupture time at each subfault is searched from a set of samples repeatedly accepted in the displacement inversion below the "critical temperature" during the cooling process of the VFSA. Such a procedure implies that the marginal a posteriori distribution of sampled parameters after the displacement inversion is utilized as a priori distribution for the velocity inversion. We then can make use of both stability in the displacement inversion and high resolution in the velocity inversion to estimate the detailed rupture propagation on the fault (Shiba, 2006).

Table 1. Search areas of model parameters used in the displacement inversion. v_r is rupture velocity and β is the S-wave velocity in the source area.

Moment ratio	0.0–5.0
Rise time (s)	0.0–3.0
v_r/β	0.6–1.0

Table 2. Search areas of model parameters used in the velocity inversion.

Effective stress ratio	0.0–10.0
Amplitude ratio of boxcar func.	0.0–5.0
v_r/β	0.6–1.0

3. Data and Initial Fault Model

Strong-motion records from ten stations, which are eight K-NET and two KiK-net surface stations, are used for the inversion. Figure 1 shows the location map of the stations along with the assumed fault plane of the main shock, the epicenter of the element event used for an empirical Green's function in the inversion analysis, and other aftershocks occurring within 24 h after the main shock. The hypocenter locations of these events are determined using the JMA unified catalog. In the initial fault model the size covering the aftershock distribution is assumed to be 36×22 km^2 (Fig. 1). I assume N58°E for the strike angle and 66° for the dip angle following the moment tensor solution of F-net (Fukuyama *et al.*, 1998). The empirical Green's function chosen in this study is an aftershock of $M_{\rm JMA}$ 4.9, which occurred on 28 March 2007 at 08:08 near the hypocenter of the main shock (and center of the assumed fault plane). The main-shock fault is divided into 19×11 subfaults 1.9 km long and wide. The size of the subfault, which is equivalent to the source area of the element event (the empirical Green's function), is determined by taking a spectral ratio of the main shock to the element event at each station (Miyake *et al.*, 2003). The corner frequency of the element event is derived from the average spectral ratio, and the equivalent source radius of the element event is estimated from the Brune's source model (Brune, 1970, 1971).

The observed acceleration records are numerically integrated to obtain data of the displacement and velocity motions, and they are band-pass-filtered from 0.1 to 2 Hz for the displacement inversion and to 5 Hz for the velocity inversion. The lower limit of the filter is determined according to the signal-to-noise ratio of the Fourier spectra for the observed element event. The S-wave portions of two horizontal ground motions are used for the inversion.

4. Inversion Results

4.1 Control parameters for inversion procedure

Tables 1 and 2 show the search areas of model parameters used in the displacement and the velocity inversions, respectively. In the inversion scheme used in this study, the search parameters, such as the moment density and the effective stress, are represented as the ratio to those of the element event. The search area of the rupture time is described as the variation of normalized rupture velocity with the S-wave velocity. In the velocity inversion, the moment ratio at each subfault is expressed as follows (Shiba and Irikura,

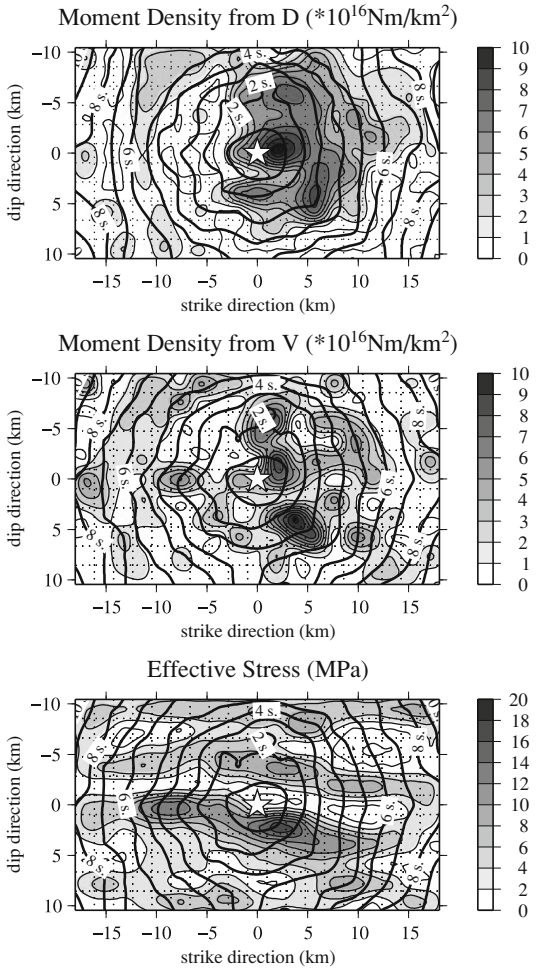

Fig. 2. Optimal source models obtained from the VFSA inversions. Upper figure shows the moment distribution derived from the displacement inversion. Middle figure and lower figure show the moment and the effective stress distributions from the velocity inversion, respectively. Contour at each figure displays the rupture time distribution.

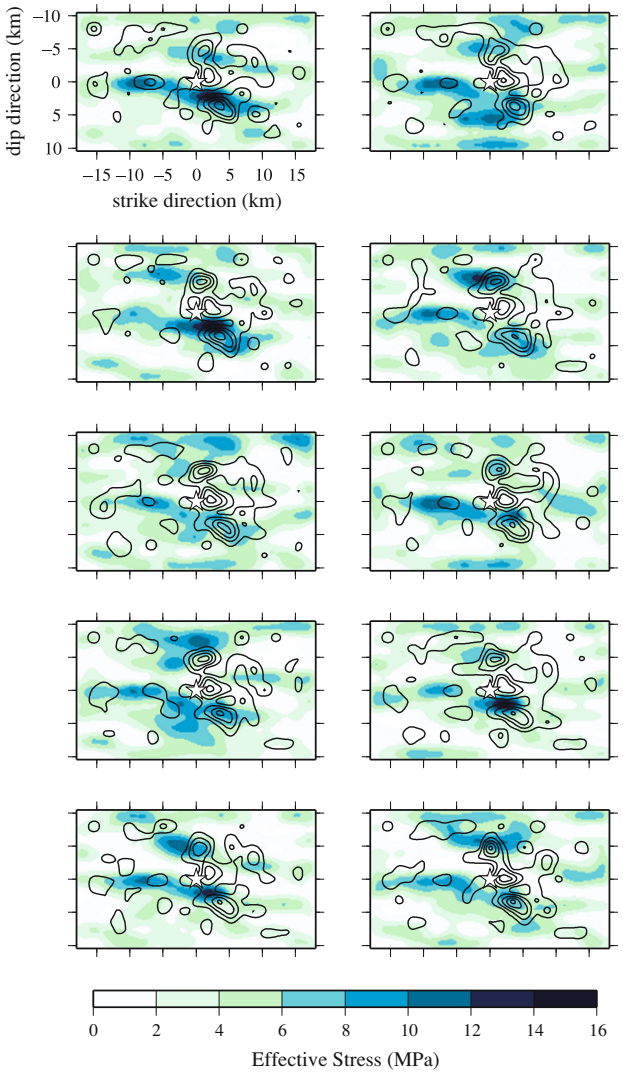

Fig. 3. Source models mapping both the moment and the effective stress distributions from 10 inversion attempts with different initial random numbers. The contour lines show the moment density and are drawn for every 2×10^{16} N m/km^2. Blue images represent the effective stress.

2005),

$$M_0/m_0 = C_1 + C_2 \cdot (N-1)\,, \tag{2}$$

where M_0 and m_0 are the moment of the main shock and the element event, respectively. C_1 is the effective stress ratio and it implies the amplitude of the delta function in the context of the filter function for the formulation of the empirical Green's function method (Irikura, 1986). C_2 implies the amplitude of the following boxcar function (or the exponentially decaying function) in the EGFM. N is the scaling parameter and is approximately equivalent to the average rise time ratio of the main shock to the element event.

Since the focal mechanism of the element event is different from that of the main shock, as shown in Fig. 1, I follow the method of Kamae *et al.* (1990) to correct the radiation pattern so as to be smoothed gradually toward the high-frequency range. In this study, the radiation coefficient obeys the theoretical value in the frequency range less than 0.5 Hz, and reaches the azimuthal average at 5 Hz as suggested in Kamae *et al.* (1990). Radiation pattern is also averaged for takeoff angles in the range from 120° to 180° (Boore and Boatwright, 1984).

The cooling schedule during the simulated annealing is written as follows (Ingber, 1989),

$$T(k) = T_0 \exp\left(-qk^p\right), \tag{3}$$

where T is the "temperature" decreasing exponentially in the cooling time k, and it controls the probability to accept the change increasing misfit. T_0 is an initial temperature, and p and q are appropriate constants adjusting the cooling speed of the system, which are determined through the test runs (preliminary inversions).

4.2 Obtained optimal solutions

Figure 2 shows the best source model for the moment distribution from the displacement inversion, and that for the moment and the effective stress distributions from the velocity inversion. They are respectively obtained from 10 inversions with different initial values for the generation of random numbers to avoid entrapment in the secondary local minima. The rupture time distribution is also contoured in Fig. 2. Note that the observed records at ISK003 and ISK005 are not used in the velocity inversion due to the

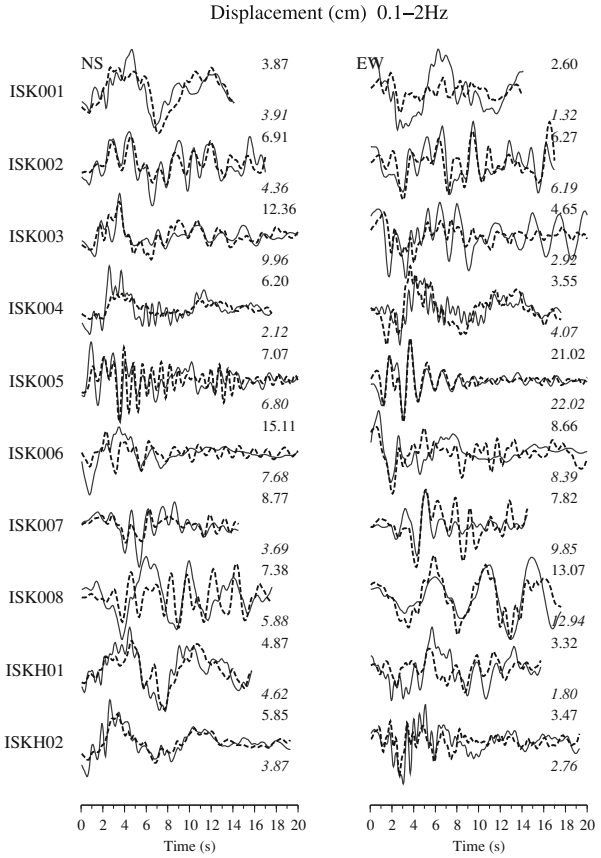

Fig. 4. Comparison of synthetic and observed displacement waveforms. Solid lines show the observed waveforms and broken lines denote synthetic ones. Numbers above the waveforms are the peak values of observed motions and those below the waveforms are the peak values of synthetics, respectively.

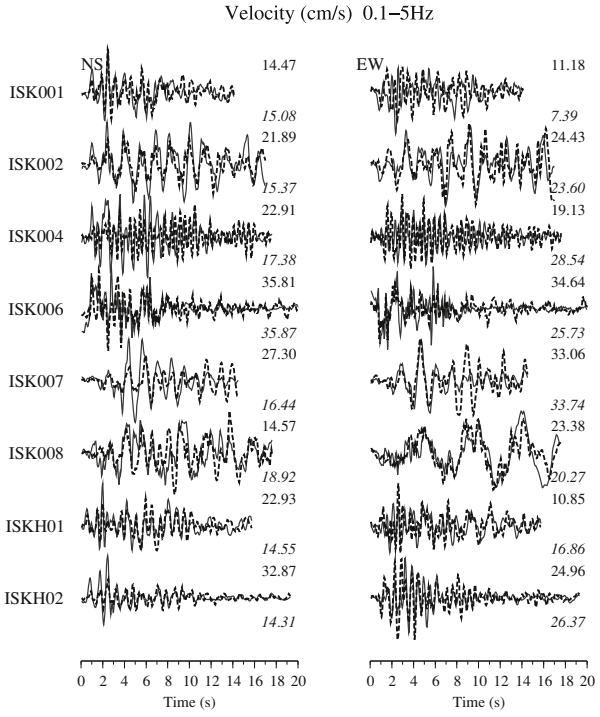

Fig. 5. Comparison of synthetic and observed velocity waveforms. Solid lines show the observed waveforms and broken lines denote synthetic ones. Numbers above the waveforms are the peak values of observed motions and those below the waveforms are the peak values of synthetics, respectively. ISK003 and ISK005 are not used in the velocity inversion.

possibility of the nonlinearity effect during the main shock. The seismic moment is released mainly from the relatively small area of 10 km long and wide in the northeast direction derived from the rupture starting point (a star in the figure). The moment and the rupture time distributions derived from the velocity inversion are very similar to that from the displacement inversion, in spite of different frequency-band and shapes of filter functions assumed in the forward process. The totally released moment is estimated to be about 1.3×10^{19} N m. The rupture velocity on the fault is rather constant except for the area just above the hypocenter, where the rupture propagation is slightly accelerated.

In contrast, the distribution of the effective stress seems to be different from that of the moment. We see the high effective stress area not only at the northeastern direction, but also in the deeper part from the hypocenter. Figure 3 shows the 10 inversion results plotting both the moment and the effective stress distributions. Though there are some differences among the obtained source models depending on the initial random number in the inversion, we can see common characteristics that the high effective stress area distributes on the shallow asperity and the periphery of the deep asperity. The deeper area of high effective stress might work as the barrier that terminates the growth of an asperity.

Figures 4 and 5 show the comparison between the synthetic motions from the best inversion solution and the observed motions for the displacement and the velocity inversions, respectively. The fits between them are generally good for both inversions.

5. Estimation of Broadband Strong Motions

The aim of the inversion scheme employed here is to demonstrate that it is possible to evaluate broadband strong motions directly from the source inversion results without any assumptions to connect the high-frequency radiation intensity and the moment distribution on the seismic source. By estimating the seismic moment and the effective stress on the fault separately, it is possible to invert the velocity motions in the frequency range up to 5 Hz successfully. Here I calculate the acceleration motions to 10 Hz, which are of engineering interest for estimating input ground motions in the seismic design, by using the optimal source models estimated from the velocity inversion along with those from the displacement inversion. The source model from the displacement inversion in this study is interpreted as the conventional model described with only the moment distribution. Therefore, the advantage of employing this proposed inversion method is verified by comparing the synthetic broadband motions from both inversions with the observed motions.

Figure 6 shows the broadband ground motions in acceleration and velocity for synthetic motions from two different inversion methods and observed motions in the frequency range from 0.1 to 10 Hz. At stations such as ISK003 (Wajima) and ISK005 (Anamizu), there are large differences between the synthetic and the observed motions, probably

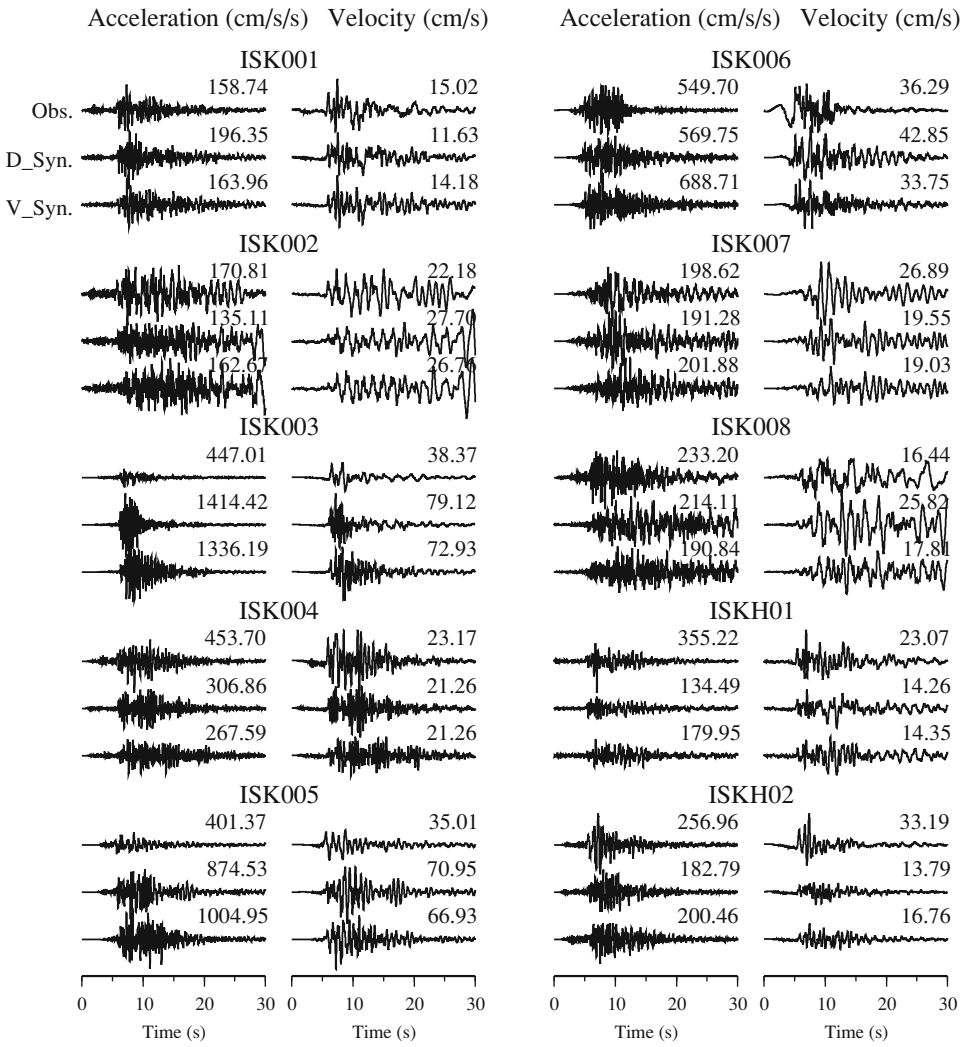

Fig. 6. Comparison of synthetic and observed motions on the NS component in the broadband frequency range from 0.1 to 10 Hz. At each station the top trace shows the observed waveform, while the middle and bottom traces indicate the synthetic motions from the displacement inversion and the velocity inversion respectively. Numbers above the waveforms are the peak values.

due to the nonlinearity effect of the sedimentary soils, as suggested earlier. For other stations, observed motions are reproduced generally well by using both inversion methods. Figure 7 shows the pseudo velocity response spectra for the observed and synthetic motions. As seen in Figs. 6 and 7, in this case, an obvious advantage over the source model based on the velocity inversion to that from conventional method cannot be shown. If there were to be a strong-motion station just near the separately existing area of higher effective stress, the difference between them might become clear. On the other hand, the strong-motion prediction based on the conventional inversion using low-frequency motions is still valid under the condition of the station distribution used in this study relative to the dimensions of the seismic source.

6. Discussion and Conclusions

In this article I applied the inversion method using very fast simulated annealing with the empirical Green's function method to the strong motion records from the 2007 Noto Hanto earthquake in order to obtain the rupture process radiating broadband ground motions. The inversion results indicate that the effective stress shows spatial distributions partly different from that of the seismic moment, suggesting barrier-like behavior which decelerates or terminates the growth of an asperity. However, the source model using the moment and effective stress variation separately estimated from the velocity inversion do not improve the synthetic acceleration motions in the frequency range up to 10 Hz and show almost same accuracy as the conventional low-frequency inversion.

Several researchers have estimated the slip distributions for this event through the inversion technique with strong-motion data (e.g. Horikawa, 2007; Iwata and Asano, 2007). Their source models commonly have one main asperity on the area including the hypocenter, which is consistent with my result. However, the asperity in the other many models is located on the shallower area from the hypocenter, while my model shows the asperity also extends to the deep direction.

For engineering purposes the characteristics of high-frequency radiation from the large earthquake are important. The recently characterized source model that systematically simplified the heterogeneous source process based on objective criterion is often applied successfully to the

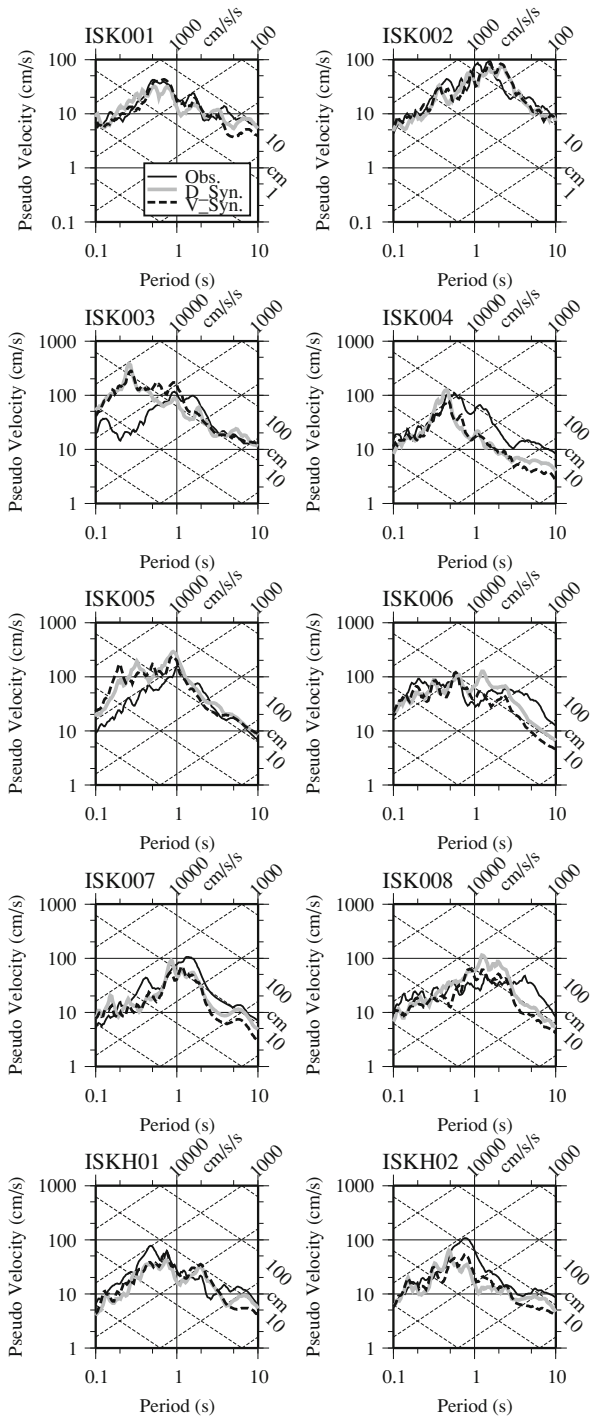

Fig. 7. Comparison of pseudo velocity response spectra ($h = 5\%$) for synthetic and observed motions on the NS component. Solid lines show the observed motions. Gray lines and broken lines are the synthetic motions from the displacement and the velocity inversions, respectively.

evaluation and/or the prediction of strong ground motions (e.g. Irikura, 2004). The idea of the source characterization is based on the reports that the asperity estimated from the low-frequency inversion corresponds to the strong motion generation area (Miyake *et al.*, 2003). The results obtained from this study suggest that the observed strong motions are well reproduced using the source model composed of only the moment distribution, though the effective stress shows the different distribution from the moment. Future works should be focused on the application of the broadband waveform inversion to the larger event such that the near-source strong motion records (just above the fault plane) are obtained at several points.

Acknowledgments. I would like to thank the K-NET, KiK-net, and F-net operated by the National Research Institute for Earth Science and Disaster Prevention (NIED) for providing the strong-motions records and moment tensor solutions. I thank the EPS reviewers and editor for their helpful comments. Figures were prepared with the Generic Mapping Tools (Wessel and Smith, 1998).

References

Akaike, H., Likelihood and the Bayes procedure, in *Bayesian Statics*, University Press, Valencia, Spain, 1980.

Aki, K., Scaling law of seismic spectrum, *J. Geophys. Res.*, **72**, 1217–1231, 1967.

Aoi, S., K. Obara, S. Hori, K. Kasahara, and Y. Okada, New strong-motion observation network: KiK-net, *Eos Trans. AGU*, 329, 2000.

Boore, D. and J. Boatwright, Average body-wave radiation coefficients, *Bull. Seismol. Soc. Am.*, **74**, 1615–1621, 1984.

Brune, J., Tectonic Stress and the Spectra of Seismic Shear Waves from Earthquakes, *J. Geophys. Res.*, **75**, 4997–5009, 1970.

Brune, J., Correction, *J. Geophys. Res.*, **76**, 5002, 1971.

Fukuyama, E., M. Ishida, D. S. Dreger, and H. Kawai, Automated seismic moment tensor determination by using on-line broadband waveforms, *Zisin 2 (J. Seismol. Soc. Jpn.)*, **51**, 149–156, 1998 (in Japanese with English abstract).

Horikawa, H., Source rupture process of 2007 Noto-Hanto Earthquake, http://unit.aist.go.jp/actfault/katsudo/jishin/notohanto/hakaikatei2.html, 2007 (in Japanese).

Ihmlé, P. F., Monte Carlo slip inversion in the frequency domain: Application to the 1992 Nicaragua slow earthquake, *Geophys. Res. Lett.*, **9**, 913–916, 1996.

Ingber, L., Very fast simulated re-annealing, *Mathl. Comput. Modelling*, **12**, 967–973, 1989.

Irikura, K., Prediction of strong acceleration motions using empirical Green's function, *Proc. 7th Jpn. Conf. Earthq. Eng.*, 151–156, 1986.

Irikura, K., Recipe for predicting strong ground motion from future large earthquake, *Ann. Disas. Prev. Res. Inst., Kyoto Univ.*, **47**, A, 2004 (in Japanese with English abstract).

Iwata, T. and K. Asano, Source process characteristics of the 2007 Noto-Hanto earthquake, *The 35th Symposium of Earthquake Ground Motion*, 7–12, 2007 (in Japanese with English abstract).

Kamae, K., K. Irikura, and Y. Fukuchi, Prediction of strong ground motion for M7 earthquake using regional scaling relations of source parameters, *J. Struct. Constr. Engng, AIJ*, **416**, 57–70, 1990 (in Japanese with English abstract).

Kinoshita, S., Kyoshin net (K-NET), *Seismol. Res. Lett.*, **69**, 309–332, 1998.

Kirkpatrick, S., C. D. Gelatt, and M. P. Vecchi, Optimization by simulated annealing, *Science*, **220**, 671–680, 1983.

Miyake, H., T. Iwata, and K. Irikura, Source characterization for broadband ground-motion simulation: Kinematic heterogeneous source model and strong motion generation area, *Bull. Seismol. Soc. Am.*, **93**, 2531–2545, 2003.

Shiba, Y. and K. Irikura, Rupture process by waveform inversion using simulated annealing and simulation of broadband ground motions, *Earth Planets Space*, **57**, 571–590, 2005.

Shiba, Y., Improvement of inversion technique with simulated annealing to estimate more accurate and well-resolved source parameters, *Programme and Abstracts, Seismol. Soc. Jpn., 2*, P068, 2006 (in Japanese).

Yoshida, S. and K. Koketsu, Simultaneous inversion of waveform and geodetic data for rupture process of the 1984 Naganoken-Seibu, Japan, earthquake, *Geophys. J. Int.*, **103**, 355–362, 1990.

Wessel, P. and W. H. F. Smith, New, improved version of Generic Mapping Tools released, *Eos Trans. AGU*, **79**, 579, 1998.

Y. Shiba (e-mail: cbar@criepi.denken.or.jp)